A Reconstruction-Classification Method for Multifrequency Electrical Impedance Tomography

Emma Malone*, Gustavo Sato dos Santos, David Holder, and Simon Arridge

***Abstract*—Multifrequency Electrical Impedance Tomography is an imaging technique which distinguishes biological tissues by their unique conductivity spectrum. Recent results suggest that the use of spectral constraints can significantly improve image quality. We present a combined reconstruction-classification method for estimating the spectra of individual tissues, whilst simultaneously reconstructing the conductivity. The advantage of this method is that *a priori* knowledge of the spectra is not required to be exact in that the constraints are updated at each step of the reconstruction. In this paper, we investigate the robustness of the proposed method to errors in the initial guess of the tissue spectra, and look at the effect of introducing spatial smoothing. We formalize and validate a frequency-difference variant of reconstruction-classification, and compare the use of absolute and frequency-difference data in the case of a phantom experiment.**

***Index Terms*—Electrical impedance tomography, electrophysical imaging, inverse methods, image reconstruction—iterative, machine learning.**

I. Introduction

ELECTRICAL IMPEDANCE TOMOGRAPHY (EIT) is an imaging method by which the conductivity of an object is recovered from measurements of the boundary voltage distribution induced by the injection of a known current. Images of live tissues and organs can be obtained by placing electrodes on the skin and injecting a small current into the body. EIT could provide a safe and cost effective alternative to established clinical imaging methods for a multitude of applications. However, the imaging problem is severely ill-posed and the resulting image quality is limited.

Extensive literature has been published on the subject of time-difference EIT, which allows for the observation of a change in conductivity which occurs over time. This technique has been successfully applied to imaging dynamic body functions such as respiration [1], gastric emptying [2] or the cardiac cycle [3]. The experimental procedure involves the acquisition of two data sets at different time points, and an image of the resulting conductivity difference is produced by inverting a linearized sensitivity model [4], [5]. The imaging problem of time-difference EIT is relatively simple, in that referring the data to a baseline reduces the sensitivity of the method to modelling and instrumentation errors [6].

Multifrequency, or multispectral, EIT is a technique for producing EIT images from static boundary voltage data, which does not require baseline measurements. Two or more data sets are acquired whilst varying the modulation frequency of the current, and biological tissues are distinguished by the unique dependence of their conductivity on frequency. The data can either be considered in its absolute form [7], [8], or sensitivity of the method to modelling errors can be reduced by referring the data against another frequency, at the cost of a reduction in contrast. With the exception of simple cases [9]–[12], MFEIT presents a more challenging imaging problem than time-difference EIT in that the absence of a linearization point forces us to solve the full nonlinear model. The value in pursuing MFEIT lies in the potential for diagnostic imaging, especially in applications which would benefit from the low cost and portability of EIT systems. For example, it has been proposed to use MFEIT for breast cancer screening [13], lung imaging [14], [15], monitoring of brain injury in intensive care [16], differentiating between stroke types in the ambulance [12], [17], [18]. However, this technique has received less attention in the literature and is at an earlier stage of development with respect to time-difference EIT.

We previously presented an MFEIT method which allows for the inclusion of explicit spectral constraints in the image reconstruction problem [19]. The proposed *fraction reconstruction method* exploits prior knowledge of the conductive properties of the tissues: the conductivity of each voxel is modelled as a linear combination of the spectra of the component tissues, multiplied by the respective volume fraction values. Given that the spatial distribution of the tissues is independent of the frequency at which measurements are taken, the tissue fractions can be reconstructed directly and simultaneously from all sets of multifrequency data. This choice brings multiple advantages; first, the introduction of spectral constraints results in a reduction in the degrees of freedom of the problem and second, it becomes possible to use frequency-difference data without increasing the number of unknowns. Results obtained in simulation and phantom experiments suggest that the use of spectral constraints yields a significant improvement in image quality with respect to pre-existing MFEIT methods.

Manuscript received December 17, 2014; revised February 05, 2015; accepted February 08, 2015. Date of publication February 11, 2015; date of current version June 29, 2015. This work was supported by the EPSRC Grant EP/J50225X/1, and the MRC Grant MR/K00767X/1. *Asterisk indicates corresponding author.*

*E. Malone is with the Department of Medical Physics and Biomedical Engineering, University College London, WC1E 6BT London, U.K. (e-mail: e.malone@ucl.ac.uk).

G. Sato dos Santos, and D. Holder are with the Department of Medical Physics and Biomedical Engineering, University College London, WC1E 6BT London, U.K.

S. Arridge is with the Department of Computer Science, University College London, WC1E 6BT London, U.K.

Color versions of one or more of the figures in this paper are available online at http://ieeexplore.ieee.org.

Digital Object Identifier 10.1109/TMI.2015.2402661

The disadvantage of the fraction reconstruction method is that exact prior knowledge of the tissue conductivities is required. This limits the application of the method to cases in which the conductivity of the tissues involved are known with a high level of accuracy. Approximate values for the tissue spectra can be obtained from the literature or *in vivo* empirical measurements, however these values are subject to variability. For example, unpredictable variations may be caused by changes in temperature, cell count, or flow-rate of bodily fluids. The fraction method treats the conductivity of a tissue at a certain frequency as a point-value, which is assumed to be known exactly and is fixed throughout the reconstruction. In this paper, a more realistic representation of the prior is obtained by associating a probability distribution to the tissue spectra. Further, we propose to use the multifrequency boundary voltage data to inform the spectral model, in addition to reconstructing the conductivity.

A similar problem in the field of diffuse optical tomography (DOT) was studied by Hiltunen *et al.* [20]. In DOT imaging, two physical quantities are recovered: light absorption and scattering. The authors proposed to exploit the covariance between the absorption and scattering parameters to perform an algorithm which alternated reconstruction and classification steps. If the result of the reconstruction step is visualized in a 2D scatter plot where the axes are the absorption and the scattering parameters, then the values form a number of clusters that is equal to the number of tissues in the domain. The voxels can therefore be classified by the clustering, and the mean and standard deviation of the tissue properties can be updated on the basis of the image. This idea can not be applied directly to EIT because there is only one reconstructed parameter, the conductivity. However, the covariance between the conductivity recovered at different frequencies can be treated in a similar way to distinguish between the tissues. The voxels can therefore be classified on the basis of the clustering of the spectra in a scatter plot of dimensions the number of frequencies.

In this paper, a method is presented for estimating the real spectra of the tissues in the domain, whilst simultaneously reconstructing an image of conductivity for each frequency. It is assumed that the domain is occupied by a finite number of tissues with distinct spectral properties, and the conductivity spectrum of each tissue is modelled by a Gaussian distribution. If each element is occupied by one, and only one, tissue, then a label can be assigned to each element. These labels constitute a hidden variable that determines the conductivity. The probability that a voxel is occupied by a certain tissue is obtained by "fuzzy labelling" the reconstructed conductivity image. The result of the labelling step is used to update the initial guess of the mean and covariance of the spectra at each iteration of the reconstruction algorithm.

We validate the proposed reconstruction-classification method on simulated data, and we test the robustness of our method to errors in the initial guess of the tissue conductivities for increasing levels of variance. We compare results obtained with and without introducing spatially smoothing regularization. We investigate the use of frequency-difference data in the reconstruction-classification method and validate the method using simulated data. The images obtained in simulation are evaluated and compared by an objective measure of quality. Finally, we apply the proposed method to experimental phantom data and compare the use of absolute and frequency-difference data.

TABLE I
GLOSSARY

σ	Conductivity
V	Boundary voltages
ω	Frequency
A	Forward map
ϵ	Real/simulated tissue spectrum
ζ	Class/tissue labels
λ	Class probability
m	Class spectrum mean
Σ	Class spectrum variance
θ	The pair (m, Σ)
γ	Regularization parameter
ρ	Reconstruction auxiliary variable
r	Responsibility

II. METHODS

A. Inverse Problem of EIT

The objective of the EIT inverse problem is to estimate the internal conductivity distribution of an object from the Neumann-to-Dirichlet map. Given the boundary voltage measurements $\boldsymbol{V}$, and assuming that the measurement noise is Gaussian distributed, an image of the conductivity $\hat{\boldsymbol{\sigma}}$ is obtained by minimizing

$$\hat{\boldsymbol{\sigma}}(\omega) = \arg\min_{\boldsymbol{\sigma}(\omega)} \frac{1}{2}\|A(\boldsymbol{\sigma}(\omega)) - \boldsymbol{V}(\omega)\|^2_{\boldsymbol{\Sigma}_V^{-1}} + R(\boldsymbol{\sigma}(\omega)), \tag{1}$$

where ω is the modulation frequency of the current, $A(\boldsymbol{\sigma}(\omega)) : \boldsymbol{\sigma}(\omega) \rightarrow \boldsymbol{V}(\omega)$ is the forward map, $\boldsymbol{\Sigma}_V$ is the covariance of the measurement noise and $R(\boldsymbol{\sigma}(\omega))$ is a regularizing function.

B. Multinomial Model

The Finite Element Model of a conductive object is considered. It is assumed that the object is composed of a finite number of tissues, and that each element of the mesh is assigned to a single tissue. A set of binary variables $\boldsymbol{\zeta}_n = \{\zeta_{n1}, \ldots, \zeta_{nj}, \ldots, \zeta_{nJ}\}$ is defined for each element, where J is the number of tissues,

$$\zeta_{nj} = \begin{cases} 1 & \text{if the } j\text{th tissue is assigned to the } n\text{th element;} \\ 0 & \text{otherwise;} \end{cases} \tag{2}$$

The values

$$\boldsymbol{\zeta}_n = \{\zeta_{n1}, \ldots, \zeta_{nj}, \ldots, \zeta_{nJ}\}$$

are drawn from a multinomial distribution $\mathrm{p}(\boldsymbol{\zeta}_n) \sim \mathrm{Multin}(1, \lambda_j)$, where λ_j is the overall probability that an element is occupied by the tissue t_j. The values of λ_j are drawn from a Dirichlet distribution $\lambda_j \sim \mathrm{Dir}(\alpha_j)$, where α_j is the

expected number of elements in the jth class. The probability that the set $\boldsymbol{\zeta}_n = \{\zeta_{n1}, \ldots, \zeta_{nj}, \ldots, \zeta_{nJ}\}$ is assigned to the nth element, given $\boldsymbol{\lambda} = \{\lambda_j;\ j = 1, \ldots, J\}$, is

$$\mathrm{p}(\boldsymbol{\zeta}_n|\boldsymbol{\lambda}) = \prod_j \lambda_j^{\zeta_{nj}}. \tag{3}$$

If the tissue t_j is assigned to the nth voxel, then it is assumed that the conductivity of the voxel at all frequencies $\boldsymbol{\sigma}_n = \{\sigma_n(\omega_i); i = 1, \ldots M\}$, where M is the number of frequencies, is given by a multivariate normal distribution

$$\begin{aligned}\mathrm{p}(\boldsymbol{\sigma}_n|\theta_j) &= \frac{1}{\sqrt{(2\pi)^J|\Sigma_j|}} \\ &\quad \times \exp\left(-\frac{1}{2}(\boldsymbol{\sigma}_n - \boldsymbol{m}_j)^T\Sigma_j^{-1}(\boldsymbol{\sigma}_n - \boldsymbol{m}_j)\right) \\ &= \mathcal{N}_\sigma(\boldsymbol{m}_j, \Sigma_j),\end{aligned} \tag{4}$$

where $\theta_j = \{(\boldsymbol{m}_j, \Sigma_j)\}$ specifies the mean $\boldsymbol{m}_j = \{m_{ij};\ i = 1, \ldots M\}$ and covariance matrix $\Sigma_j \in \mathbb{R}^{M\times M}$ of the spectrum of the jth tissue. Therefore, if the indicator variables ζ_{nj} are known, the probability distribution of the conductivities of the nth voxel is

$$\mathrm{p}(\boldsymbol{\sigma}_n|\boldsymbol{\zeta}_n, \boldsymbol{\theta}) = \prod_j \left(\mathrm{p}(\boldsymbol{\sigma}_n|\theta_j)\right)^{\zeta_{nj}}. \tag{5}$$

The joint probability of recovering $(\boldsymbol{\sigma}_n, \boldsymbol{\zeta}_n)$ is

$$\mathrm{p}(\boldsymbol{\sigma}_n, \boldsymbol{\zeta}_n|\boldsymbol{\theta}, \boldsymbol{\lambda}) = \mathrm{p}(\boldsymbol{\sigma}_n|\boldsymbol{\zeta}_n, \boldsymbol{\theta})\mathrm{p}(\boldsymbol{\zeta}_n|\boldsymbol{\lambda}) = \prod_j \left[\lambda_j \mathrm{p}(\boldsymbol{\sigma}_n|\theta_j)\right]^{\zeta_{nj}}. \tag{6}$$

By marginalizing over all possible values of the indicator variables ζ_{nj} the *mixture of Gaussians* model for the conductivity is obtained

$$\mathrm{p}(\boldsymbol{\sigma}_n|\boldsymbol{\theta}, \boldsymbol{\lambda}) = \int_{\boldsymbol{\zeta}_n} \mathrm{p}(\boldsymbol{\sigma}_n, \boldsymbol{\zeta}_n|\boldsymbol{\theta}, \boldsymbol{\lambda})\mathrm{d}\boldsymbol{\zeta}_n = \sum_j \lambda_j \mathrm{p}(\boldsymbol{\sigma}_n|\theta_j). \tag{7}$$

Using a non-informative prior for the means $\mathrm{p}(\boldsymbol{m}_j) \propto 1$, the conjugate prior distribution for the covariances is given by the *normal inverse Wishart distribution*

$$NIW(\nu_j, \Gamma_j) = |\Sigma_j|^{-(\nu+d+1)/2} \exp\left[-\frac{1}{2}\mathrm{Tr}\left(\Gamma_j\Sigma_j^{-1}\right)\right], \tag{8}$$

where d is the dimension of the domain, ν_j indicates the number of degrees of freedom, and Γ_j is a scaling matrix. If the prior is non-informative, $\nu_j = 0$ and $\Gamma_j = 0$, so that

$$\mathrm{p}(\Sigma_j) = |\Sigma_j|^{-(d+1)/2}, \tag{9}$$

which is known as Jeffreys prior.

C. Combined Reconstruction-Classification Outline

A set of boundary voltage measurements $\boldsymbol{V}_i = \{V_{ki};\ k = 1, \ldots, K\}$ is acquired at each frequency $\{\omega_i;\ i = 1, \ldots, M\}$. The conductivity distribution can be recovered iteratively by alternating a reconstruction and a classification step

1) Reconstruction:

$$\boldsymbol{\sigma}^{t+1} = \arg\min_{\boldsymbol{\sigma}} \frac{1}{2}\|L_V(A(\boldsymbol{\sigma}) - \boldsymbol{V})\|^2 - \frac{1}{2}\log \mathrm{p}(\boldsymbol{\sigma}|\boldsymbol{\zeta}^t, \boldsymbol{\theta}^t), \tag{10}$$

where $\boldsymbol{\sigma} \in \mathbb{R}^{N\cdot M}$ accounts for N voxels and M frequencies, $\|\cdot\|$ indicates the Frobenious norm, and L_V is a weighting matrix.

2) Classification:

$$\mathrm{E-step}: \qquad \boldsymbol{\zeta}^{t+1} = \arg\max_{\boldsymbol{\zeta}} \mathrm{p}(\boldsymbol{\zeta}|\boldsymbol{\sigma}^t, \boldsymbol{\theta}^t, \boldsymbol{\lambda}^t) \tag{11}$$

$$\mathrm{M-step}: (\boldsymbol{\theta}^{t+1}, \boldsymbol{\lambda}^{t+1}) = \arg\max_{(\boldsymbol{\theta}, \boldsymbol{\lambda})} \mathrm{p}(\boldsymbol{\sigma}^t|\boldsymbol{\theta}, \boldsymbol{\lambda})\mathrm{p}(\boldsymbol{\theta}, \boldsymbol{\lambda}). \tag{12}$$

D. Reconstruction

Substituting (5) into (10) and assuming that the elements are independent, the objective function becomes

$$\boldsymbol{\sigma} = \arg\min_{\boldsymbol{\sigma}} \frac{1}{2}\|L_V(A(\boldsymbol{\sigma}) - \boldsymbol{V})\|^2 - \frac{1}{2}\sum_{n,j} \zeta_{nj}\log \mathrm{p}(\boldsymbol{\sigma}_n|\theta_j), \tag{13}$$

where

$$\begin{aligned}\boldsymbol{V} &= \{\boldsymbol{V}_1; \ldots, \boldsymbol{V}_i; \ldots; \boldsymbol{V}_M\} \in \mathbb{R}^{K\cdot M} \\ A(\boldsymbol{\sigma}) &= \{A(\boldsymbol{\sigma}_1); \ldots; A(\boldsymbol{\sigma}_i); \ldots; A(\boldsymbol{\sigma}_M)\} \in \mathbb{R}^{K\cdot M}.\end{aligned}$$

The weighting matrix L_V, of dimensions $\mathbb{R}^{K\cdot M\times K\cdot M}$, holds the values $1/(\sqrt{2M}\|A(\boldsymbol{\sigma}_i^0) - \boldsymbol{V}_i\|)$ on the diagonal, where $\boldsymbol{\sigma}^0$ is the initial guess for the conductivity, and serves the purpose of equilibrating the contribution of each frequency to the reconstruction. We assume that the measurement noise is not correlated across frequencies, therefore the off-diagonal values are all zero.

The regularization term is found by fixing the value of the indicator parameters $\boldsymbol{\zeta}$ to the *maximum-a-posteriori* estimate recovered by the previous classification step

$$\mathrm{MAP}(\boldsymbol{\zeta}) = \arg\max_{\boldsymbol{\zeta}} \mathrm{p}(\boldsymbol{\zeta}|\boldsymbol{\sigma}^{t-1}, \boldsymbol{\theta}^{t-1}, \boldsymbol{\lambda}^{t-1}). \tag{14}$$

The result of the MAP estimate is a binary image with only 0 or 1 values, where for each voxel the label corresponding to the tissue that has highest probability of occupying the voxel is set to one, and all other labels are set to 0. The expected spectrum of the nth element becomes

$$\bar{\boldsymbol{\sigma}}_n = \sum_j \zeta_{nj}\cdot m_{ij}\Big|_{\mathrm{MAP}(\boldsymbol{\zeta})} = m_{ij'} \quad i = 1, \ldots, M \tag{15}$$

if the j'th tissue has maximum probability of being assigned to the nth element. Therefore (5) becomes

$$\mathrm{p}(\boldsymbol{\sigma}|\boldsymbol{\zeta}, \boldsymbol{\theta}) = \prod_n \prod_j \mathrm{p}(\boldsymbol{\sigma}_n|\theta_j)^{\zeta_{nj}} = \mathcal{N}_\sigma(\bar{\boldsymbol{\sigma}}, \boldsymbol{\Sigma}_{\bar{\sigma}}), \tag{16}$$

where $\bar{\boldsymbol{\sigma}} \in \mathbb{R}^{N\cdot M}$ and $\boldsymbol{\Sigma}_{\bar{\sigma}} \in \mathbb{R}^{N\cdot M\times N\cdot M}$ is a sparse matrix of which the nth $M\times M$ block along the diagonal is $\boldsymbol{\Sigma}_{j'}$ if the nth elements belongs to the j'th class.

The conductivity at all frequencies is thus obtained from (10) by minimizing,

$$\boldsymbol{\sigma} = \arg\min_{\boldsymbol{\sigma}} \frac{1}{2}\|L_V(A(\boldsymbol{\sigma}) - \boldsymbol{V})\|^2 + \frac{\gamma}{2}\underbrace{\|L_{\bar{\sigma}}(\boldsymbol{\sigma} - \bar{\boldsymbol{\sigma}})\|^2}_{R_{\bar{\sigma}}(\boldsymbol{\sigma})}, \tag{17}$$

where γ is a regularization parameter and $L_{\bar{\sigma}} \in \mathbb{R}^{N\cdot M\times N\cdot M}$ is the Cholesky decomposition of of $\boldsymbol{\Sigma}_{\bar{\sigma}}^{-1}$.

Positivity is enforced by introducing an auxiliary variable $\boldsymbol{\rho}$ such that $\rho_{ni} = \log(\sigma_{ni})\ \forall\, n, i$. The objective function is expressed in terms of the variable $\boldsymbol{\rho}$, and the derivatives are computed using the chain rule. At the reconstruction step t, the problem is initialized to the result of the previous classification step $\bar{\boldsymbol{\sigma}}^t$, the corresponding auxiliary variable is computed, and one step of damped Gauss-Newton descent [21] is performed to obtain $\boldsymbol{\rho}^{t+1}$. Finally, the result of the reconstruction step is

$$\sigma_{ni}^{t+1} = \exp\left(\rho_{ni}^{t+1}\right) > 0 \quad \forall\, n, i.$$

E. Classification

The classification step computes the expected values for the labels (E-step), and updates the tissue-class spectral parameters $(\boldsymbol{\theta}, \boldsymbol{\lambda})$ (M-step), given the conductivity image $\boldsymbol{\sigma}^t$.

1) E-Step: The *responsibility* r_{nj}^t is a measure of the probability that the nth voxel is occupied by the jth tissue

$$\begin{aligned}\mathrm{p}(\zeta_{nj} = 1|\boldsymbol{\sigma}_n, \boldsymbol{\theta}^t, \boldsymbol{\lambda}^t) &= \frac{\mathrm{p}(\boldsymbol{\sigma}_n|\zeta_{nj}=1, \boldsymbol{\theta}^t)\mathrm{p}(\zeta_{nj}=1)}{\mathrm{p}(\boldsymbol{\sigma}_n|\boldsymbol{\theta}, \boldsymbol{\lambda})} \\ &= \frac{\lambda_j^t \mathrm{p}\left(\boldsymbol{\sigma}_n^t|\theta_j^t\right)}{\sum_j \lambda_j^t \mathrm{p}\left(\boldsymbol{\sigma}_n^t|\theta_j^t\right)} \\ &= r_{nj}^t \end{aligned} \tag{18}$$

The expectation for the indicator values is

$$\begin{aligned} E(\zeta_{nj}|\boldsymbol{\sigma}_n, \boldsymbol{\theta}^t, \boldsymbol{\lambda}^t) &= \int \zeta_{nj}\mathrm{p}(\zeta_{nj}=1|\boldsymbol{\sigma}_n, \boldsymbol{\theta}^t, \boldsymbol{\lambda}^t)\,\mathrm{d}\zeta_{nj} \\ &= 0 * \mathrm{p}(\zeta_{nj}=0|\boldsymbol{\sigma}_n, \boldsymbol{\theta}^t, \boldsymbol{\lambda}^t) \\ &\quad + 1 * \mathrm{p}(\zeta_{nj}=1|\boldsymbol{\sigma}_n, \boldsymbol{\theta}^t, \boldsymbol{\lambda}^t) \\ &= r_{nj}^t \end{aligned} \tag{19}$$

Therefore the MAP estimate for the labels, and the solution to (14), is

$$\zeta_{nj}^{t+1} = \begin{cases} 1 & \text{if} r_{nj}^t \text{is maximum}\ \forall j, \\ 0 & \text{otherwise.} \end{cases} \tag{20}$$

2) M-Step: The parameters $(\boldsymbol{\theta}, \boldsymbol{\lambda})$ are chosen in order to maximize the log posterior (12)

$$(\boldsymbol{\theta}^{t+1}, \boldsymbol{\lambda}^{t+1}) = \arg\max_{(\boldsymbol{\theta}, \boldsymbol{\lambda})} \log \mathrm{p}(\boldsymbol{\sigma}^t|\boldsymbol{\theta}, \boldsymbol{\lambda}) + \log \mathrm{p}(\boldsymbol{\theta}, \boldsymbol{\lambda}) \tag{21}$$

Averaging over all possible values of $\boldsymbol{\zeta}$ gives

$$\begin{aligned}&\log \mathrm{p}(\boldsymbol{\sigma}^t|\boldsymbol{\theta}, \boldsymbol{\lambda}) + \log \mathrm{p}(\boldsymbol{\theta}, \boldsymbol{\lambda}) \\ &\qquad = \int_{\zeta} \log \mathrm{p}(\boldsymbol{\sigma}^t, \boldsymbol{\zeta}|\boldsymbol{\theta}, \boldsymbol{\lambda})\mathrm{d}\zeta + \log \mathrm{p}(\boldsymbol{\theta}, \boldsymbol{\lambda}) \end{aligned} \tag{22}$$

Using *Jensen's inequality* [22] and ignoring terms which do not depend on $(\boldsymbol{\theta}, \boldsymbol{\lambda})$, we obtain a lower bound for the log-prior

$$\begin{aligned}&\mathcal{B}(\boldsymbol{\theta}, \boldsymbol{\lambda}) \\ &\quad = \sum_n \sum_j r_{nj}^t \log\left(\lambda_j \mathrm{p}(\boldsymbol{\sigma}_n|\theta_j)\right) + \log \mathrm{p}(\boldsymbol{\lambda}) + \log \mathrm{p}(\boldsymbol{\theta}) \\ &\quad = \sum_n \sum_j r_{nj}^t \Big[\log(\lambda_j) + \log(|\Sigma_j|) \\ &\qquad -\frac{1}{2}(\boldsymbol{\sigma}_n - \boldsymbol{m}_j)'\Sigma_j^{-1}(\boldsymbol{\sigma}_n - \boldsymbol{m}_j)\Big] \\ &\qquad + \sum_j \left[(\alpha_j - 1)\log(\lambda_j) - \frac{\nu_j + d + 1}{2}\log|\Sigma_j|\right] \end{aligned} \tag{23}$$

Maximizing $\mathcal{B}(\boldsymbol{\theta}, \boldsymbol{\lambda})$ for $\sum_j \lambda_j = 1$ and using the mode of the Dirichlet distribution for λ_j, returns the update rules for the parameters,

$$\lambda_j^{t+1} = \frac{\sum_n r_{nj}^t + (\alpha_j - 1)}{N + \sum_j \alpha_j - J} \tag{24}$$

In the case of a non-informative priors $\alpha_j = 1$ and $\mathrm{p}(\boldsymbol{m}_j) \propto 1$

$$\lambda_j^{t+1} = \frac{\sum_n r_{nj}^t}{N}, \tag{25}$$

$$\boldsymbol{m}_j^{t+1} = \frac{\sum_n r_{nj}^t \boldsymbol{\sigma}_n}{\sum_n r_{nj}^t}, \tag{26}$$

$$\Sigma_j^{t+1} = \frac{\sum_n r_{nj}^t (\boldsymbol{\sigma}_n - \boldsymbol{m}_j)(\boldsymbol{\sigma}_n - \boldsymbol{m}_j)^T + \Gamma_j}{\sum_n r_{nj}^t + \nu_j + d + 1}. \tag{27}$$

F. Frequency-Difference Combined Reconstruction-Classification Outline

The class parameters $\theta_j^{\mathrm{fd}} = \{(\boldsymbol{m}_j^{\mathrm{fd}}, \Sigma_j^{\mathrm{fd}})\}$ specify the mean and covariance matrix of the *relative* spectrum of the jth tissue:

$$\boldsymbol{m}_j^{\mathrm{fd}} \equiv \{m_{2j} - m_{1j}; \ldots, m_{ij} - m_{1j}; \ldots; m_{Mj} - m_{1j}\} \quad \forall j,$$

where the lowest frequency ω_1 is chosen as reference.

The conductivity distribution is recovered by performing a reconstruction step using frequency-difference data, calculating the frequency-difference conductivity images, and following with a classification step

1) Frequency-difference reconstruction:

$$\boldsymbol{\sigma}^{t+1} = \arg\min_{\boldsymbol{\sigma}} \frac{1}{2}\left\|L_V^{\mathrm{fd}}(A^{\mathrm{fd}}(\boldsymbol{\sigma}) - \boldsymbol{V}^{\mathrm{fd}})\right\|^2 - \frac{1}{2}\log \mathrm{p}(\boldsymbol{\sigma}^{\mathrm{fd}}|\boldsymbol{\zeta}^t, \boldsymbol{\theta}^{\mathrm{fd},t}, \boldsymbol{\lambda}^t), \tag{28}$$

where $\boldsymbol{V}^{\mathrm{fd}}$ is the set of frequency-difference data. The frequency-difference conductivity images are given by:

$$\boldsymbol{\sigma}^{\mathrm{fd}} = \{\boldsymbol{\sigma}_i - \boldsymbol{\sigma}_1\ \forall i = 2, \ldots, M\} \tag{29}$$

2) Frequency-difference classification:

$$\mathrm{E-step}: \boldsymbol{\zeta}^{t+1} = \arg\max_{\boldsymbol{\zeta}} \mathrm{p}(\boldsymbol{\zeta}|\boldsymbol{\sigma}^{\mathrm{fd},t}, \boldsymbol{\theta}^{\mathrm{fd},t}, \boldsymbol{\lambda}^t) \tag{30}$$

M-step:

$$(\boldsymbol{\theta}^{\mathrm{fd},t+1}, \boldsymbol{\lambda}^{t+1}) = \arg\max_{(\boldsymbol{\theta}^{\mathrm{fd}}, \boldsymbol{\lambda})} \mathrm{p}(\boldsymbol{\sigma}^{\mathrm{fd},t}|\boldsymbol{\theta}^{\mathrm{fd}}, \boldsymbol{\lambda})\mathrm{p}(\boldsymbol{\theta}^{\mathrm{fd}}, \boldsymbol{\lambda}). \tag{31}$$

G. Frequency-Difference Reconstruction

The reconstruction problem is modified from the absolute case to use data referred to a baseline frequency. If data is normalized by the reference the norm of the residual error becomes

$$\sum_{i=2}^{M} \frac{1}{2} \left\| L_V^i \left(\frac{A(\boldsymbol{\sigma}_i) - A(\boldsymbol{\sigma}_1)}{A(\boldsymbol{\sigma}_1)} - \frac{\boldsymbol{V}_i - \boldsymbol{V}_1}{\boldsymbol{V}_1} \right) \right\|^2 = \frac{1}{2} \left\| L_V^{\mathrm{fd}} (A^{\mathrm{fd}}(\boldsymbol{\sigma}) - \boldsymbol{V}^{\mathrm{fd}}) \right\|^2, \quad (32)$$

where L_V^{fd} hold the values

$$L_V^i = 1 \Bigg/ \left(\sqrt{2(M-1)} \left\| \frac{A\left(\boldsymbol{\sigma}_i^0\right) - A\left(\boldsymbol{\sigma}_1^0\right)}{A\left(\boldsymbol{\sigma}_1^0\right)} - \frac{\boldsymbol{V}_i - \boldsymbol{V}_1}{\boldsymbol{V}_1} \right\| \right) \quad \forall i = 2, \ldots, M$$

on the diagonal,

$$\boldsymbol{V}^{\mathrm{fd}} = \left\{ \frac{\boldsymbol{V}_2 - \boldsymbol{V}_1}{\boldsymbol{V}_1}; \ldots, \frac{\boldsymbol{V}_i - \boldsymbol{V}_1}{\boldsymbol{V}_1}; \ldots; \frac{\boldsymbol{V}_M - \boldsymbol{V}_1}{\boldsymbol{V}_1} \right\} \in \mathbb{R}^{K \cdot (M-1)},$$

and

$$A^{\mathrm{fd}}(\boldsymbol{\sigma}) = \left\{ \frac{A(\boldsymbol{\sigma}_2) - A(\boldsymbol{\sigma}_1)}{A(\boldsymbol{\sigma}_1)}; \ldots; \frac{A(\boldsymbol{\sigma}_i) - A(\boldsymbol{\sigma}_1)}{A(\boldsymbol{\sigma}_1)}; \ldots; \frac{A(\boldsymbol{\sigma}_M) - A(\boldsymbol{\sigma}_1)}{A(\boldsymbol{\sigma}_1)} \right\} \in \mathbb{R}^{K \cdot (M-1)}.$$

The result of the previous classification step provides an approximated prior for the difference of the conductivity with respect to the reference frequency:

$$R_{\bar{\sigma}}(\boldsymbol{\sigma}) = \gamma \left\| L_{\bar{\sigma}}^{\mathrm{fd}} (\boldsymbol{\sigma}^{\mathrm{fd}} - \bar{\boldsymbol{\sigma}}^{\mathrm{fd}}) \right\|^2. \quad (33)$$

where

$$\boldsymbol{\sigma}^{\mathrm{fd}} = \{ \boldsymbol{\sigma}_2 - \boldsymbol{\sigma}_1; \ldots; \boldsymbol{\sigma}_i - \boldsymbol{\sigma}_1; \ldots; \boldsymbol{\sigma}_M - \boldsymbol{\sigma}_1 \} \in \mathbb{R}^{N \cdot (M-1)}, \quad (34)$$

and

$$\bar{\boldsymbol{\sigma}}^{\mathrm{fd}} = \sum_j \zeta_{nj} \cdot m_{ij}^{\mathrm{fd}} \Big|_{\mathrm{MAP}(\boldsymbol{\zeta})} = m_{ij'}^{\mathrm{fd}} \quad i = 2, \ldots, M. \quad (35)$$

H. Frequency-Difference Classification

The reconstruction problem using difference data is no longer unique, however tissue-based clustering is observed in difference images given by $\boldsymbol{\sigma}_i - \boldsymbol{\sigma}_1 \ \forall i = 2, \ldots, M$. Therefore the classification algorithm is performed on the set of images $\boldsymbol{\sigma}^{\mathrm{fd}}$ (34) and the parameters of the relative spectra are updated. The implementation is otherwise the same as for the case of using absolute data.

I. Spatial Smoothing

Spatial smoothing is introduced by adding a regularization term to the objective function (17),

$$\boldsymbol{\sigma} = \arg\min_{\boldsymbol{\sigma}} \frac{1}{2} \| L_V (A(\boldsymbol{\sigma}) - \boldsymbol{V}) \|^2 + \frac{\gamma_1}{2} R_{\mathrm{s}}(\boldsymbol{\sigma}) + \frac{\gamma_2}{2} \| L_{\bar{\sigma}} (\boldsymbol{\sigma} - \bar{\boldsymbol{\sigma}}) \|^2, \quad (36)$$

where $R_{\mathrm{s}}(\boldsymbol{\sigma})$ assumes the general form of a Markov Random field

$$R_{\mathrm{s}}(\boldsymbol{\sigma}) = \sum_{i,n,m} w_{nl(n)} \Psi(|\sigma_{ni} - \sigma_{l(n)i}|), \quad (37)$$

where $l(n)$ runs over the neighbours of the nth voxel, $w_{nl(n)}$ is a weighting factor, and Ψ indicates a function of $|\sigma_{ni} - \sigma_{l(n)i}|$. In this paper we choose $\Psi = |\sigma_{ni} - \sigma_{l(n)i}|^2$ and either $w_{nl(n)} = 1$ (homogeneous MRF) or $w_{nl(n)} = \boldsymbol{\zeta}_n^T \cdot \boldsymbol{\zeta}_{l(n)}$ (label-dependent MRF).

J. Image Quality Evaluation

Three measures of error are considered in order to evaluate the quality of images recovered from simulated data. The first is the L_2-norm of the difference between the recovered conductivity $\boldsymbol{\sigma}^{\mathrm{recon}}$ and the numerical phantom $\boldsymbol{\sigma}^{\mathrm{true}}$, expressed as a ratio of the norm of the model and divided by the number of frequencies:

$$\mathrm{Err}_{L_2} = \frac{1}{M} \sum_{i=1}^{M} \frac{\|\boldsymbol{\sigma}_i^{\mathrm{recon}} - \boldsymbol{\sigma}_i^{\mathrm{true}}\|}{\|\boldsymbol{\sigma}_i^{\mathrm{true}}\|}. \quad (38)$$

The second is the classification error $\mathrm{Err}_{\mathrm{class}}$, given by the percentage of misclassified elements in the mesh. The third is the mean error committed in approximating the spectra of the tissue classes:

$$\mathrm{Err}_{\mathrm{spctr}} = \frac{1}{M} \frac{1}{T} \sum_{i,j} \frac{|m_{ij} - \epsilon_{ij}|}{\epsilon_{ij}}, \quad (39)$$

where ϵ indicates the simulated conductivities of the tissues and m the means of the tissue conductivities recovered by the last classification step.

To evaluate images recovered from experimental data, the mean across frequencies of the contrast-to-noise ratio (CNR) is considered. Given a tissue t_j, $\mathrm{CNR}(j)$ is defined as

$$\mathrm{CNR}(j) = \frac{1}{M} \sum_{i=1}^{M} \frac{\left[\sigma_i^{p(j)} - \sigma_i^b \right]^2}{\mathtt{std}\left(\sigma_i^b\right)^2}, \quad (40)$$

where `std` indicates the standard deviation, and $\sigma_i^{p(j)}$ and σ_i^b are the mean values of the image across the areas corresponding to, respectively, the perturbation made of the tissue t_j and the background. In the case of simulated data, the positions of the background and the perturbations are known exactly, and in the case of experimental data, the positions are estimated by measuring the location of the perturbations.

K. Visualization of Scatter Plots and Responsibility

Conductivity images are displayed alongside scatter plots and responsibility images. The axis of the scatter plots are the projections onto the primary and secondary basis vectors of the conductivity images, which are obtained by taking the SVD decomposition of the matrix $\boldsymbol{\sigma} \in \mathbb{R}^{N \cdot M}$. Each point on the scatter plots corresponds to the projections a_1 and a_2 of the vector of conductivity values assumed for all frequencies by each voxel $\boldsymbol{\sigma}_{ni} = \{\sigma_{ni}; i = 1, \ldots M\}$. The responsibility images display

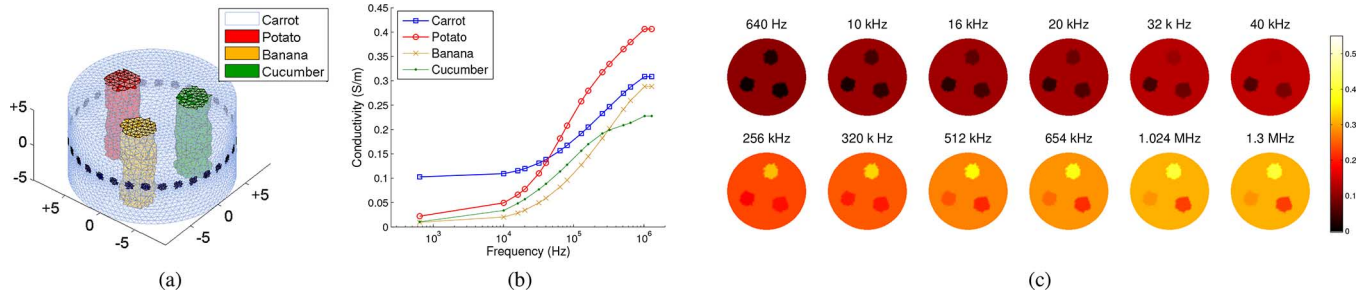

Fig. 1. Numerical phantom: (a) mesh and location of the inclusions (axis units are cm), (b) conductivity spectra of the tissues ϵ, (c) model conductivity for all frequencies.

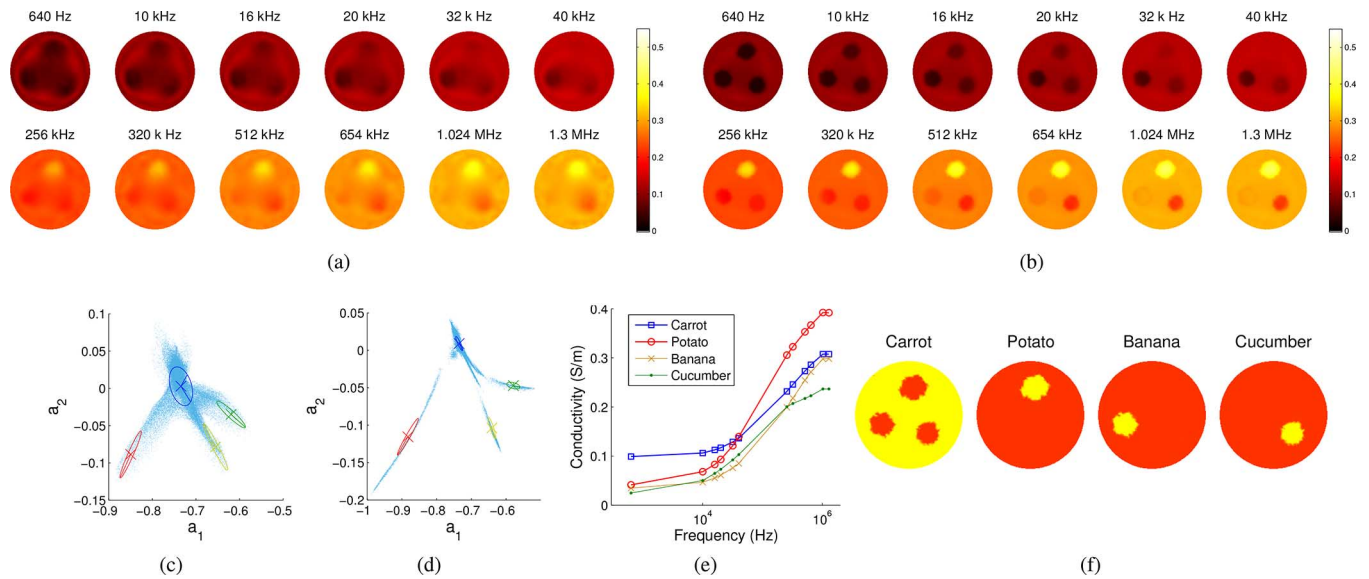

Fig. 2. Reconstruction-classification with homogeneous MRF: conductivity recovered at (a) iteration 1 and (b) iteration 6 (final); scatter plots (Section II.K) of the projection onto the primary a_1 and secondary a_2 basis vectors of the conductivity images at (c) iteration 1 and (d) iteration 6 (the cross indicates the mean and the ellipse represents the variance of the classes and the colour map is: blue-carrot, red-potato, yellow-banana, green-cucumber); (e) mean conductivity spectra m and (f) responsibility (the probability that the element is assigned to a certain tissue) recovered at final iteration (Section II.K).

the probability that each voxel is assigned to a certain tissue, as defined by (18).

III. Results

A. Experimental Design

In the following, we present the results of application of the proposed reconstruction-classification method to numerical (III.B) and experimental data. The method was validated on simulated data (III.C), and the robustness to errors in the initial guess of the tissue conductivities was tested for increasing levels of variance (III.D). The use of spatial smoothing in addition to the spectral prior in the reconstruction step was investigated. Images obtained using homogeneous MRF regularization were compared to results obtained with no spatial smoothing (III.E) and with a label-dependent MRF (III.F). The use of frequency-difference data in the reconstruction-classification method was investigated and the method was validated using simulated data (III.G). The images obtained in simulation were evaluated and compared by an objective measure of quality (III.H). Finally, a phantom experiment was performed to compare the use of absolute and frequency-difference data in the reconstruction-classification method (III.I).

B. Numerical Phantom and Data Simulation

A numerical phantom was created using a cylindrical mesh with approximately 62 000 elements, of diameter 19 cm and height 10 cm. 32 electrodes were placed in a ring around the middle of the tank, and a further electrode was placed at the centre of the base and connected to ground. Three cylindrical inclusions of radius 2.2 cm and height 10 cm were located in a homogeneous background. The inclusions were positioned in (0.87 cm 4.92 cm), (-4.7 cm -1.71 cm), and (3.83 cm -3.21 cm). The background tissue was a mixture of 0.1% concentration saline and carrot pieces, and the inclusions were composed of, respectively, potato, banana and cucumber (Fig. 1(a)). The tissue spectra were obtained by measuring the conductvity of samples using a Hewlett-Packard 42847A (Hewlett-Packard, CA, USA) impedance analyser. Twelve EIT measurement frequencies were chosen in the range 640 Hz–1.3 MHz (Fig. 1(b) and (c)). Current of amplitude 133 μA was injected through polar electrodes, and the voltage differences accross adjacient pairs were considered. Proportional 0.1% white Gaussian noise was added to the simulated data:

$$\boldsymbol{V}^{\text{with noise}} = \boldsymbol{V}^{\text{no noise}}(1+h) \tag{41}$$

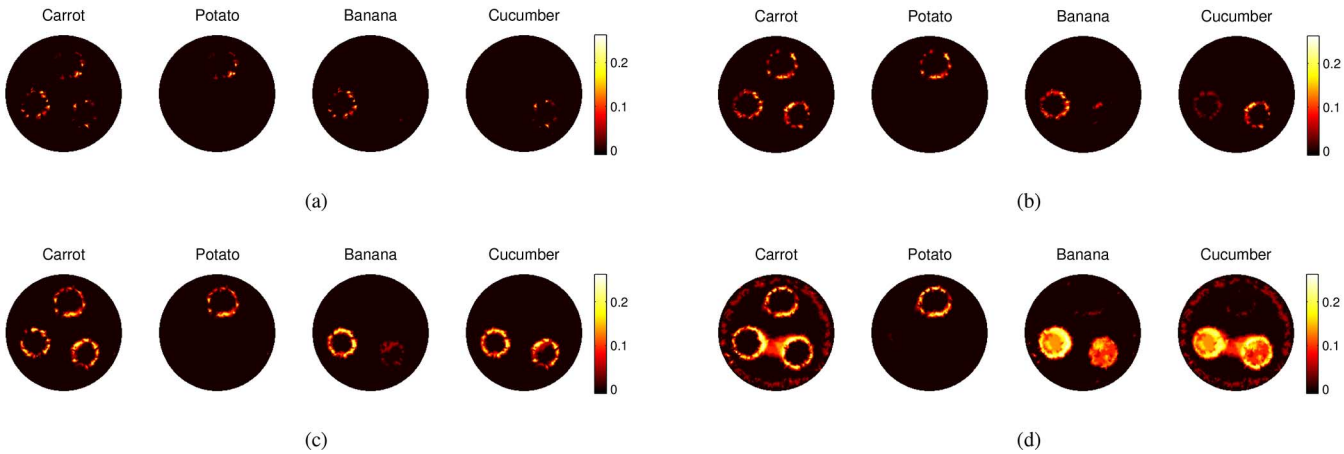

Fig. 3. Robustness to error errors in the initial guess of the tissue spectra: images of variance over 20 trials of the labels obtained after adding errors to the tissue spectra with variance 1% (a), 5% (b), 10% (c) and 20% (d).

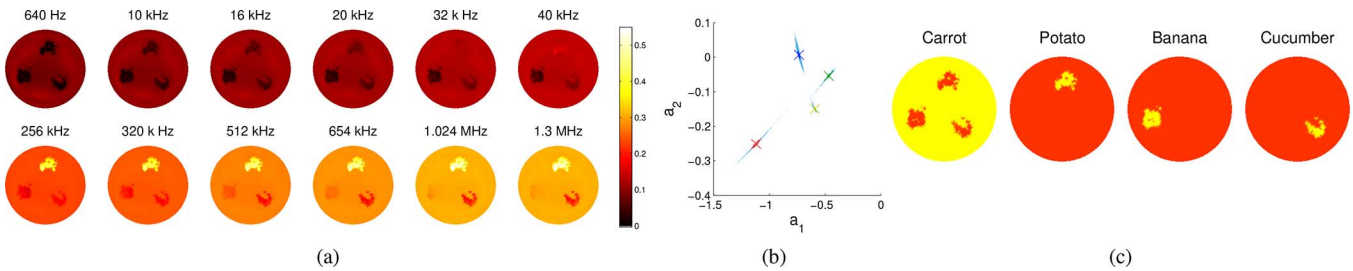

Fig. 4. Reconstruction-classification in the case of independent elements: (a) conductivity, (b) and scatter plot at final iteration and (c) responsability (Section II.K).

where $h \sim \mathcal{N}(0, \varsigma)$ indicates a random number drawn from a Gaussian distribution with zero mean and standard deviation $\varsigma = 0.1 \cdot 10^{-2}$.

C. Reconstruction-Classification Method With Homogeneous MRF Regularization: Numerical Validation

Images were reconstructed using the reconstruction-classification method (Fig. 2). The number of iteration was fixed at 6 in all the following cases. Homogeneous Markov Random Field (hMRF) smoothing was applied (see (37))

$$R_s(\boldsymbol{\sigma}) = \gamma_1 \sum_{i,n,l(n)} |\sigma_{ni} - \sigma_{l(n)i}|^2. \tag{42}$$

The initial mean values of the spectra were set to the real simulated spectra ϵ (Fig. 1(b)), and the covariance was set to $\boldsymbol{\Sigma}_j = 10^{-3}\mathbf{I}$ for all four tissues. The parameters of the inverse Wishart distribution were set to $\nu_1 = 20000$ and $\Gamma_j = 10^{-2}\mathbf{I}$ for the background, and $\nu_j = 5000$ and $\Gamma_j = 10^{-1}\mathbf{I}$ for the other tissues. The regularization parameters were set to $\gamma_1 = 10^{-4}$ and $\gamma_2 = 10^{-8}$. In all cases the values of the regularization parameters were chosen by varying γ_1 and γ_2 independently within a range of $[10^{-3}, 10^{-5}]$ for γ_1 and $[10^{-7}, 10^{-9}]$ for γ_2, and testing logarithmically spaced points. The spatial parameter γ_1 was set to the value which gave the lowest error in the simulated conductivity images (38) or the highest CNR in the experimental conductivity images (40). The spectral parameter γ_2 was chosen so that the conductivity of the tissues would converge to the mean of the classes over approximately 6 iterations. If γ_2 is too high, the classification stagnates after a small number of iterations, and if γ_2 is too low the spectral information is not used efficiently and contrast is lost. Therefore the value of γ_2 must be low enough to allow for the spectral model to vary while the estimation of the image improves, and high enough for the conductivity of the tissues to approach the mean in the final iteration.

D. Robustness to Spectral Errors

A study was performed to test the robustness of the reconstruction-classification method to errors in the initial guess of the spectra of the tissues. Errors were added to the conductivity value of each tissue before simulating the boundary voltage data at each frequency. Gaussian distributed errors were chosen with mean the value of the spectra used in the reconstruction ϵ (Fig. 1(b)), and the study was repeated for increasing variance values: 1%, 5%, 10% and 20%. For each variance, the errors were sampled and the reconstruction was repeated 20 times. The parameters of the reconstruction-classification algorithm were set to those used in the numerical validation. Results for the voxel-wise variance of the MAP estimate of the labels over 20 draws are presented (Fig. 3).

E. Reconstruction-Classification With Independent Elements

Images were reconstructed without spatial smoothing. The initial covariance was set to $\boldsymbol{\Sigma}_j = 10^{-3}\mathbf{I}$ for all tissues. The parameters of the inverse Wishart distribution were set to the same values as in Section III.B. The regularization parameter was $\gamma_2 = 10^{-8}$ (and, obviously, $\gamma_1 = 0$, $R_s = 0$), and 6 iterations were performed (Fig. 4).

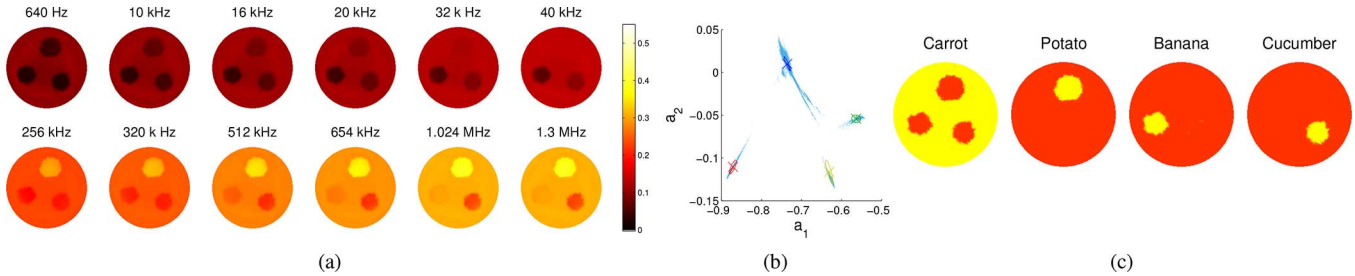

Fig. 5. Reconstruction-classification with label-dependent MRF: (a) conductivity, (b) and scatter plot at final iteration and (c) responsability (Section II.K).

F. Reconstruction-Classification With Label-Dependant MRF Regularization

Images were reconstructed using the result of the classification step to qualify the regularization in the successive reconstruction step. The Markov Random Field regularization term is modified so that only neighbours with the same expected tissue labels, as given by (14), are considered. The MRF term becomes (37)

$$R_s(\boldsymbol{\sigma}) = \gamma_1 \sum_{i,n,l(n)} \left({\boldsymbol{\zeta}_n^t}^T \cdot \boldsymbol{\zeta}_{l(n)}^t \right) |\sigma_{ni} - \sigma_{l(n)i}|^2,$$

where $\boldsymbol{\zeta}_n^t$ indicates the labels assigned at the previous iteration, and

$${\boldsymbol{\zeta}_n^t}^T \cdot \boldsymbol{\zeta}_{l(n)}^t = \begin{cases} 1 & \text{if } \zeta_{nj}^t = \zeta_{l(n)j}^t \ \forall j, \\ 0 & \text{otherwise.} \end{cases} \tag{43}$$

The parameters of the reconstruction-classification algorithm were set to the same values used in III.B. Images of the numerical phantom were reconstructed by performing 6 iterations of reconstruction-classification (Fig. 5).

G. Frequency-Difference Reconstruction-Classification: Numerical Validation

The first classification step was set up using the result of the first reconstruction step: the initial guess for the mean and variance of the classes was set to that of the region of the image corresponding to each tissue. The parameters of the inverse Wishart distribution were set to $\nu_1 = 20\,000$ and $\Gamma_j = 10^{-2}\mathbf{I}$ for the background, and $\nu_j = 5000$ and $\Gamma_j = 10^{-1}\mathbf{I}$ for perturbation. Label-dependent MRF regularization was applied, and the regularization parameters were set to $\gamma_1 = 10^{-4}$ and $\gamma_2 = 10^{-8}$, and 6 iterations were performed (Fig. 6).

H. Image Quality Evaluation and Convergence

The results obtained using the reconstruction classification method with homogeneous MRF regularization (Section III.C, Fig. 2), independent elements (Section III.E, Fig. 4), label-dependent MRF regularization (Section III.F, Fig. 5), and frequency-difference data with label-dependent MRF regularization (Section 6, Fig. 6) were evaluated by our image quantification method (Section II.J) and compared (Fig. 7(a)). Similarly, we compared the results of our study (Section III.D, Fig. 3) of the robustness of the reconstruction-classification method to errors added to the initial guess of the tissue spectra (Fig. 7(b)). In all cases the number of iterations was fixed to 6. Convergence of the algorithm was evaluated in terms of the descent of the classification error $\mathrm{Err}_{\mathrm{class}}$ over the number of iterations of reconstruction and classification steps. Results obtained for different choices of regularization (Fig. 8(a)) and after adding errors to the initial estimates of the tissue spectra (Fig. 8(b)) were compared.

I. Phantom Experiment

A phantom was obtained using a perspex cylindrical tank that was modelled by the mesh used in simulation. The tank was filled with a mixture of 0.1% concentration saline solution and carrot cubes of approximately 4 mm side. A potato with a diameter of approximately 4.6 cm and length 10 cm was placed first in position (-4 cm 0 cm 0 cm) (Fig. 9(a)), and then in (0 cm $+4$ cm 0 cm) (Fig. 9(e)). The conductivity spectra of the sample tissues were the same as used in simulation ϵ (Section III.B, Fig. 1(b)). Boundary voltage measurements were recorded with the UCLH Mark 2.5 MFEIT system and using an array of silver electrodes. The measurement protocol was the same as for the simulation case (see III.B), and measurements were averaged over 10 frames.

The initial mean of the spectra was set to values measured with the impedance analyzer, and the covariance was set to $\boldsymbol{\Sigma}_j = 10^{-2}\mathbf{I}$ for the background, and $\boldsymbol{\Sigma}_j = 10^{-3}\mathbf{I}$ for the perturbation. The parameters of the inverse Wishart distribution were set to $\nu_1 = 10^6$ and $\Gamma_j = 10^{-1}\mathbf{I}$ for the background, and $\nu_j = 20000$ and $\Gamma_j = 10^{-3}\mathbf{I}$ for perturbation. Images were reconstructed using absolute (Fig. 9) and frequency-difference (Fig. 10) data using label-dependent MRF regularization. The regularization parameters were set to $\gamma_1 = 10^{-4}$, $\gamma_2 = 10^{-8}$ for absolute data and $\gamma_1 = 10^{-3}$, $\gamma_2 = 10^{-8}$ for frequency-difference data. Six iterations of both reconstruction and classification steps were performed in all cases. The images were evaluated objectively by calculating the average over frequencies of the contrast-to-noise ratio of the perturbation in the conductivity images. Using absolute data the mean CNR was 9.3 and 9.61 respectively for positions (-4 cm 0 cm 0 cm) and (0 cm $+4$ cm 0 cm), and using frequency-difference data the CNR was significantly lower at 3.22 and 5.

IV. Discussion

A. Numerical Results Obtained With Homogeneous MRF, Independent Elements and Label-Dependent MRF

The choice of introducing homogeneous Markov Random field regularization had the effect of increasing the error on the estimation of the tissue spectra. This was visible in the "streaking" between the clusters in the scatter plots (see Fig. 2).

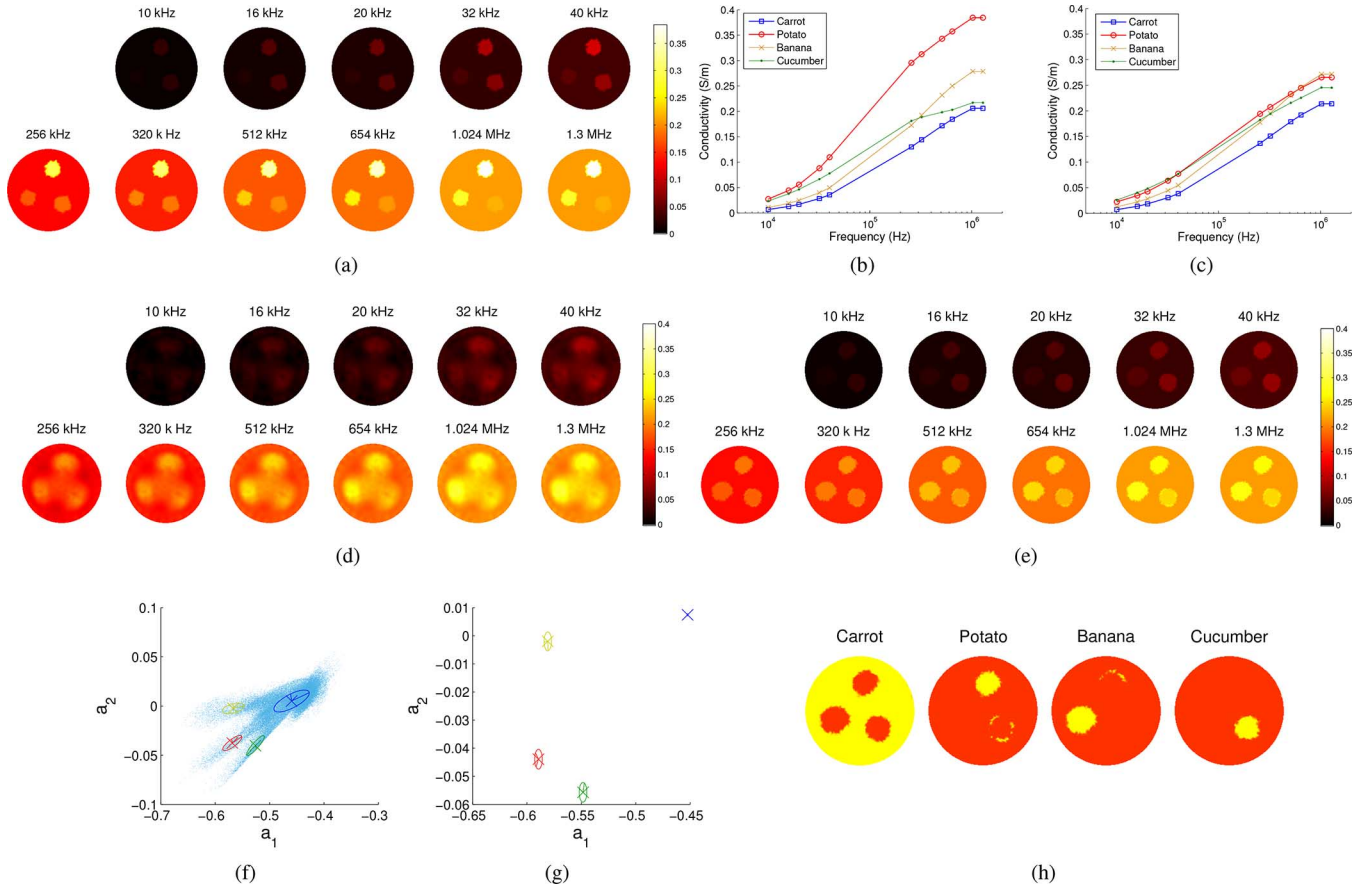

Fig. 6. Frequency-difference reconstruction-classification model and results: (a) frequency-difference conductivity model for all frequencies; (b) relative frequency-difference conductivity spectra of the tissues ϵ^{fd}; (c) mean frequency-difference conductivity spectra m^{fd} recovered by the reconstruction-classification method; frequency-difference conductivity images obtained at (d) iteration 1 and (e) iteration 6 (final); scatter plots at (f) iteration 1 and (g) iteration 6; (h) responsibility at final iteration (Section II.K).

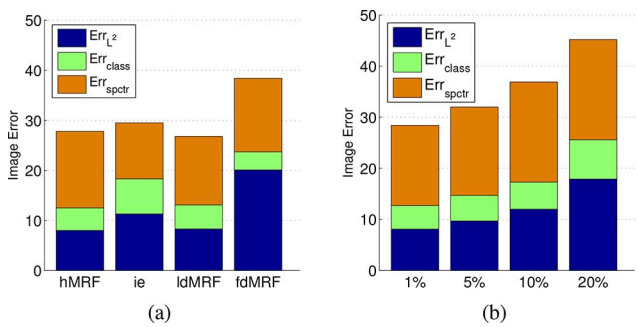

Fig. 7. Image quality of numerical results: (a) reconstruction classification method with homogeneous MRF (hMRF), independent elements (ie), label-dependent MRF (ldMRF), and frequency-difference with label-dependent MRF (fdMRF); (b) mean over 20 repetitions of the image quality obtained after 1%, 5%, 10% and 20% adding errors to the initial guess of the spectra.

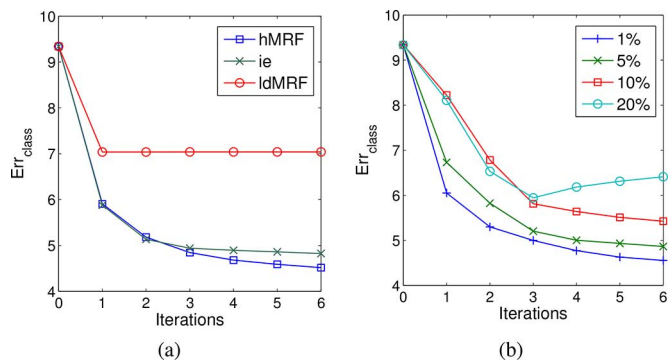

Fig. 8. Convergence analysis: descent of the classification error over the number of iterations for (a) reconstruction classification method with homogeneous MRF (hMRF), independent elements (ie) and label-dependent MRF (ldMRF); and (b) after adding 1%, 5%, 10% and 20% errors to the initial guess of the spectra.

The reason for this is that the hMRF regularization favours spatially smooth solutions. Therefore, instead of a jump-change in the conductivity of areas assigned to different tissues, elements along the boundary between tissues assumed intermediate conductivity values. These elements caused an increase in the covariance associated to the tissue classes. In the final image, the largest eigenvalue of the covariance of each perturbation class corresponded to the direction of the line joining the mean conductivity of the perturbation to that of the background. However, from the comparison with the case of independent elements (no spatial smoothing, Fig. 4) it was evident that the use of hMRF regularization had the effect of significantly improving the overall image quality, as reflected by the reduction in the L_2-norm and the classification errors (Fig. 7(a)). Indeed, in the case of independent elements the classification error

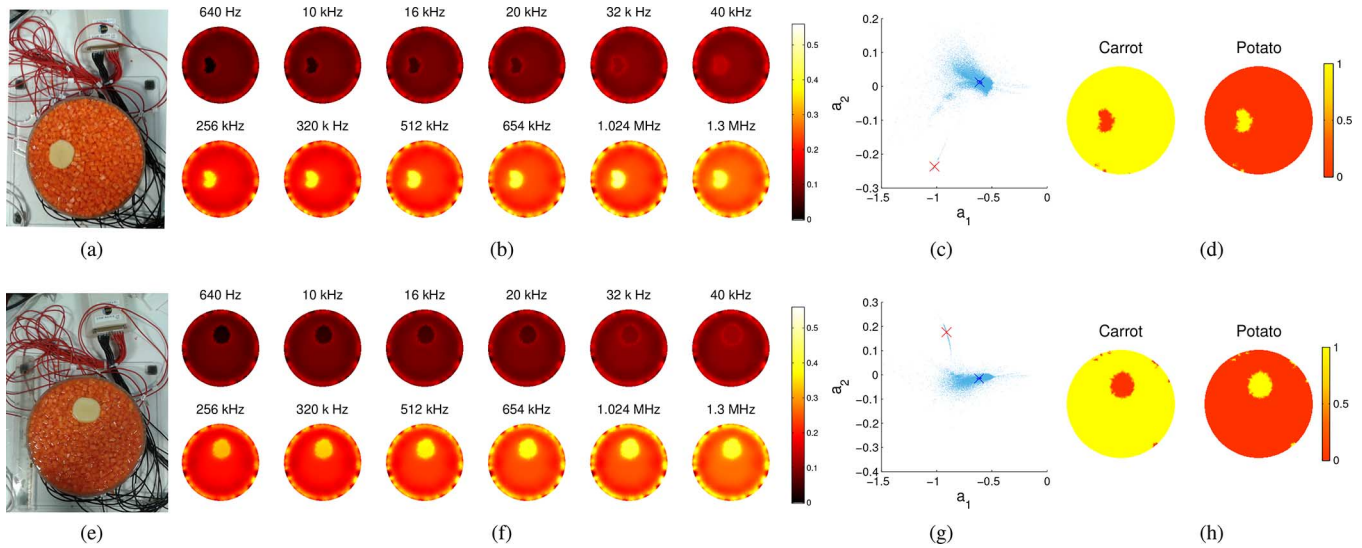

Fig. 9. Phantom experiment setup and reconstruction-classification results for absolute data: (a) experimental setup, (b) conductivity image and (c) scatter plot and (d) responsibility image for position (−4 cm 0 cm 0 cm); (e) experimental setup, (f) conductivity image, (g) scatter plot and (h) responsibility image for position (0 cm +4 cm 0 cm) (Section II.K). The conductivity images (b) and (f) present boundary artefacts arising from modelling errors in the position of the electrodes.

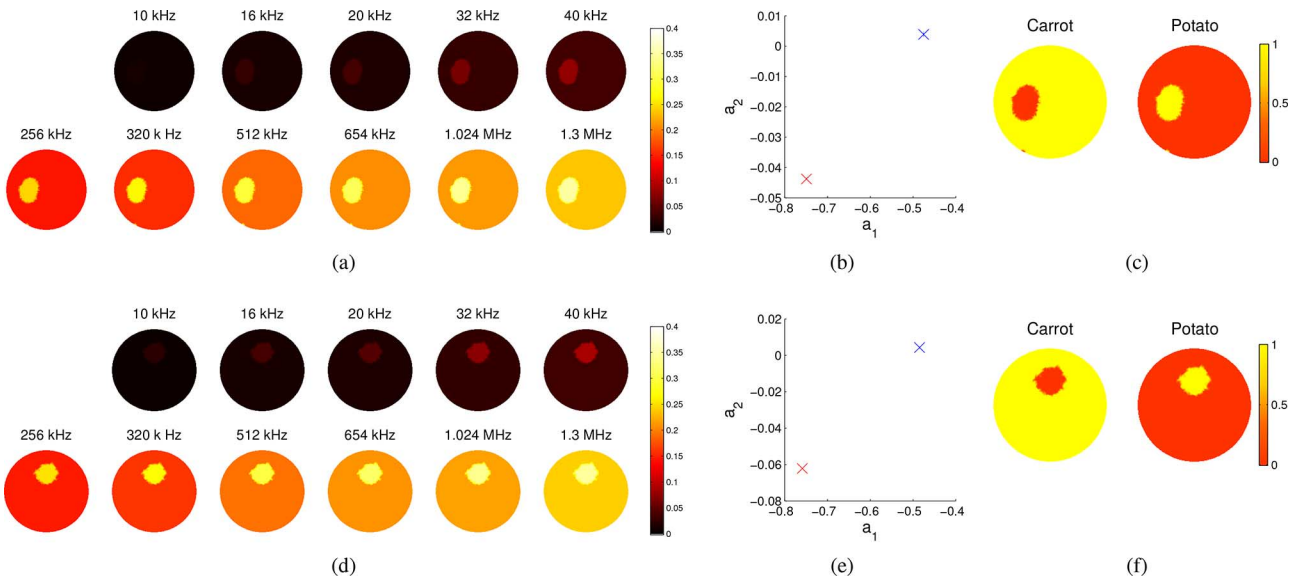

Fig. 10. Phantom experiment reconstruction-classification results for frequency-difference data: (a) conductivity image and (b) scatter plot and (c) responsibility image for position (−4 cm 0 cm 0 cm); (d) conductivity image, (e) scatter plot and (f) responsibility image for position (0 cm +4 cm 0 cm) (Section II.K). The boundary artefact is suppressed in the conductivity images (a) and (d) by use of frequency-difference data.

stagnates after one iteration (Fig. 8(a)), indicating that the use of the spectral model alone is insufficient to correctly segment the conductivity images.

The choice to use the result of the classification step to qualify the successive reconstruction step by using label-dependant MRF allowed for sharp edges between tissues whilst favouring large homogeneous areas (Fig. 5). Neighbouring voxels that were assigned to different tissues in the previous classification step were not considered in the calculation of the regularization term; therefore elements lying along the edge between tissues assumed the conductivity of one or the other tissue. This modification returned an improvement in the spectral errors with respect to hMRF (Fig. 7(a)).

B. Robustness to Spectral Errors

The variance of the images obtained after adding errors to the initial guess of the tissue spectra was found to be very low. For 1% error, the images were nearly unchanged, and for 20% error the maximum variation in the images with the respect to the mean was only 1.9% (Fig. 3). This result indicated that the classification step corrected the estimate of the tissue properties. The image quality was found to be dependant on the spectral error, and the imaging errors increased with the variance of the spectral error (Fig. 7(b)). Further, convergence of the algorithm was slower for larger spectral errors (Fig. 8(b)), which suggests that a higher number of iterations may be required if the initial estimate for the spectra is far away from the real values.

C. Frequency-Difference Combined Reconstruction-Classification

The advantage of using frequency-difference data in the image reconstructions was that the result was more robust to modelling errors. The sensitivity of the method to errors in the geometry of the boundary, the localization and shape of the electrodes, and contact impedance is higher if absolute data is used. In an experimental setup, this may result in severe edge artifact, which can significantly affect image quality. The effect of referring the data to a low frequency is the suppression frequency-independent modelling and instrumentation errors, in the same way that the use of time-difference data allows for the suppression of time-independent errors.

The disadvantage to using frequency difference data is that the number of data points is reduced from $K \cdot M$ to $K \cdot (M-1)$, whereas the number of unknown remains constant N. Also, the reconstruction problem is no longer unique. We therefore do not expect the reconstructed absolute values to agree with the simulated model. Therefore, tissues are distinguished only by the difference in the relative slope of the spectrum, rather that the absolute conductivity values, and this can result in a loss in contrast.

In conducting the simulation study (Section III.G, Figs. 6 and 7(a)), it proved difficult to perform the correct classification of the tissues when the class means were initialized to the expected values ϵ, and the class variances were set to a multiple of the identity matrix. The reason for this is that the conductivity values recovered by the first reconstruction step were too distant from the real values. Instead, we adopted the method used in [20], and chose to initialize the parameters using the result of the first reconstruction step. This required knowledge of the approximate location of the perturbation tissues, which may either be held *a priori*, or may also be gained from the first reconstruction result. In this case the data was simulated, and the region of interest corresponding to the location of each tissues was already known. However in an experimental setup it would have been necessary to view the first reconstructed image and select the areas corresponding to significant perturbations. This could be achieved either manually, by visualizing the result, or by choosing an automatic criterion. For example, the image could be thresholded to consider voxels with significant variations from the background value as "other than the background tissue". Then the perturbation tissues could be distinguished by finding neighbouring clusters of voxels, and considering each cluster as a distinct tissue.

D. Computation Time

The run time of the proposed reconstruction algorithm was approximately 20 minutes per iteration on a 16 core workstation with 128 GB RAM. The majority of the computation time was spent finding the solution to the forward problem and the update search direction for the inverse problem. There is scope for optimizing the imaging method in order to minimize run time and memory usage. For example, recent advances in the development of parallelized solvers could allow for a reduction in the forward solve time for large scale problems [23]. This could enable the choice of a memory efficient inversion method that requires a larger number of iterations, such as limited-memory BFGS [24]. Alternatively, introducing a suitable pre-conditioner could improve the solve time of the Gauss-Newton search direction. Further, integration with the approximation error method could also allow for the use of lower-resolution meshes without loss of image quality [25], [26].

E. Phantom Experiment

The phantom experiment was designed to highlight the effect of using frequency-difference data in the reconstruction. The images recovered from absolute data (Fig. 9) presented a ring-shaped artefact around the edge of the tank. This was caused by the mismatch between the model and the real shape of the boundary and electrodes, electrode localization, contact impedance, and instrumentation errors [7], [27]. The errors were most evident near the electrodes because the sensitivity to noise is highest in the areas where the current density is highest.

The use of frequency-difference data allowed for the subtraction of frequency-invariant errors in the data, and thus resulted in the suppression of the boundary artefact (Fig. 10). However, information about the absolute values of the conductivity of the tissues was lost, and the recovered contrast was lower with respect to the case of absolute data (Section III.I). As the observer is likely to be most sensitive to the appearance of the artefacts, the use of frequency-difference data has the effect of improving the overall visual quality of the image. However, the images obtained from absolute data contain relatively more information about the conductivity of the object, and perform better in terms of an objective evaluation measure.

V. Conclusion

We have formalized, validated and applied a combined reconstruction-classification method for Multifrequency Electrical Impedance Tomography. The novelty of the method lies in the simultaneous estimation of the conductivity and the spectra of the tissues in the domain. This allows for the use of the spectral information in the reconstruction step, while the constraints are updated in the classification step to correct possible errors in the initial assumptions.

We have found that our method is very robust to errors in the initial guess of the tissue spectra. We have compared alternative choices of regularization and concluded that it is preferable to introduce spatial smoothing, and that edges can be enhanced by using the classification result to inform the regularization in the reconstruction step. We have formalized and validated a frequency-difference variant of the method. We have applied absolute and frequency-difference reconstruction-classification to phantom data collected in a tank, and found that the use of frequency-difference data results in the suppression of edge artefacts, but also results in a reduction in contrast.

The assumption of a Gaussian statistical model for the tissue spectra results in the inclusion of a second order regularization term in the objective function for the conductivity. Given that the latter is differentiable, the problem can then be solved relatively easily by applying a gradient descent method. In our phantom experiment, measurements of the tissue samples acquired with the impedance spectroscoper were consistent with

a Gaussian distribution. In the event that the conductivity spectrum of a particular tissue were found to be non-Gaussian, the method could be modified to include an appropriate statistical model.

Further work is necessary to compare the performance of the reconstruction classification method using absolute and frequency-difference data. The results are likely to be dependant on the spectra of the tissues involved, and on the distance of the anomalies from the electrodes. Further analysis is required to investigate the robustness of the method to modelling errors such as erroneous electrode location and contact impedance. The method could also be improved by modifying the prior distribution of the spectral properties of the tissues to include information about cross-frequency correlation. Our results suggest that the proposed method is suitable for applications involving a number of tissues with inaccurately known spectra. Future work will focus on applying reconstruction-classification to image *in vivo* tissues in an animal model.

ACKNOWLEDGMENT

The authors would like to thank Simon Prince for providing many of the original ideas explored in this paper.

REFERENCES

[1] J. Mueller, D. Isaacson, and J. Newell, "Reconstruction of conductivity changes due to ventilation and perfusion from EIT data collected on a rectangular electrode array," *Physiol. Meas.* vol. 97, 2001 [Online]. Available: http://iopscience.iop.org/0967-3334/22/1/313

[2] Y. Mangnall, A. Baxter, and R. Avill, "Applied potential tomography: A new noninvasive technique for assessing gastric function," *Clin. Phys. Physiol. Meas.* vol. 119, 2001 [Online]. Available: http://iopscience.iop.org/0143-0815/8/4A/016

[3] B. M. Eyuboglu, B. H. Brown, and D. C. Barber, "In vivo imaging of cardiac related impedance changes," *IEEE Eng. Med. Biol. Mag.* vol. 8, no. 1, pp. 39–45, Jan. 1989.

[4] W. Lionheart, N. Polydorides, and A. Borsic, "The reconstruction problem," in *Electr. Impedance Tomogr.*, 2004, pp. 3–64.

[5] W. Lionheart, "EIT reconstruction algorithms: Pitfalls, challenges and recent developments," *Physiol. Meas.* vol. 25, no. 1, pp. 125–142, Feb. 2004.

[6] A. McEwan, G. Cusick, and D. S. Holder, "A review of errors in multi-frequency EIT instrumentation," *Physiol. Meas.* vol. 28, no. 7, pp. S197–215, Jul. 2007.

[7] V. Kolehmainen, M. Vauhkonen, P. Karjalainen, and J. Kaipio, "Assessment of errors in static electrical impedance tomography with adjacent and trigonometric current patterns," *Physiol. Meas.* vol. 18, no. 4, p. 289, 1997.

[8] L. Horesh *et al.*, "Beyond the linear domain—The way forward in MFEIT image reconstruction of the human head," in *IFMBE Proc.*, Poland, 2004, vol. 3, no. 11, pp. 683–686.

[9] J. K. Seo, J. Lee, S. W. Kim, H. Zribi, and E. J. Woo, "Frequency-difference electrical impedance tomography (fdEIT): Algorithm development and feasibility study," *Physiol. Meas.* vol. 29, no. 8, pp. 929–944, Aug. 2008.

[10] S. C. Jun *et al.*, "Frequency-difference electrical impedance tomography (fdEIT): Validation by simulation and tank experiment," *Physiol. Meas.* vol. 30, no. 10, pp. 1087–1099, Oct. 2009.

[11] S. Ahn, T. I. Oh, S. C. Jun, J. K. Seo, and E. J. Woo, "Validation of weighted frequency-difference EIT using a three-dimensional hemisphere model and phantom," *Physiol. Meas.* vol. 32, no. 10, pp. 1663–1680, Oct. 2011.

[12] B. Packham *et al.*, "Comparison of frequency difference reconstruction algorithms for the detection of acute stroke using EIT in a realistic head-shaped tank," *Physiol. Meas.* vol. 33, no. 5, pp. 767–786, May 2012.

[13] A. Malich *et al.*, "Electrical impedance scanning as a new imaging modality in breast cancer detectiona short review of clinical value on breast application, limitations and perspectives," *Nucl. Instrum. Methods Phys. Res.* vol. 497, no. 1, pp. 75–81, Jan. 2003.

[14] A. R. Hampshire, R. H. Smallwood, B. H. Brown, and R. A. Primhak, "Multifrequency and parametric EIT images of neonatal lungs," *Physiol. Meas.* vol. 16, no. 3A, pp. A175–A189, Aug. 1995.

[15] B. H. Brown, A. D. Leathard, L. Lu, W. Wang, and A. Hampshire, "Measured and expected Cole parameters from electrical impedance tomographic spectroscopy images of the human thorax," *Physiol. Meas.* vol. 16, no. 3A, pp. A57–A67, Aug. 1995.

[16] X. Shi *et al.*, "Preliminary research on monitoring of cerebral ischemia using electrical impedance tomography technique," in *IEEE EMBS Annu. Int. Conf.*, Jan. 2008, vol. 2008, pp. 1188–1191.

[17] L. Horesh *et al.*, "Stroke type differentiation by multi-frequency electrical impendance tomography—A feasibility study," in *IFMBE Proc.*, 2005, vol. 12.

[18] A. Romsauerova *et al.*, "Multi-frequency electrical impedance tomography (EIT) of the adult human head: Initial findings in brain tumours, arteriovenous malformations and chronic stroke, development of an analysis method and calibration," *Physiol. Meas.* vol. 27, no. 5, pp. S147–S161, May 2006.

[19] E. Malone, G. Sato Dos Santos, D. Holder, and S. Arridge, "Multifrequency electrical impedance tomography using spectral constraints," *IEEE Trans. Med. Imag.* vol. 33, no. 2, pp. 340–350, Oct. 2013.

[20] P. Hiltunen, S. J. D. Prince, and S. Arridge, "A combined reconstruction-classification method for diffuse optical tomography," *Phys. Med. Biol.* vol. 54, no. 21, pp. 6457–6476, Nov. 2009.

[21] L. Horesh, M. Schweiger, S. Arridge, and D. Holder, "Large-scale non-linear 3D reconstruction algorithms for electrical impedance tomography of the human head," in *IFMBE Proc.*, 2007, vol. 14, pp. 3862–3865.

[22] S. Prince, *Computer Vision: Models, Learning, and Inference*. Cambridge, U.K.: Cambridge Univ. Press, 2012.

[23] M. Jehl, A. Dedner, T. Betcke, and K. Aristovich, "A fast parallel solver for the forward problem in electrical impedance tomography," *IEEE Trans. Biomed. Eng.*, vol. 62, no. 1, pp. 126–137, Jan. 2015.

[24] J. Nocedal and S. Wright, *Numerical Optimization*. New York: Springer-Verlag, 1999, Operat. Res. Financial Eng..

[25] J. Kaipio and E. Somersalo, *Statistical and Computational Inverse Problems*. New York: Springer, 2005.

[26] A. Nissinen, L. M. Heikkinen, and J. P. Kaipio, "The Bayesian approximation error approach for electrical impedance tomography experimental results," *Meas. Sci. Technol.* vol. 19, no. 1, p. 015501, Jan. 2008.

[27] A. Boyle and A. Adler, "The impact of electrode area, contact impedance and boundary shape on EIT images," *Physiol. Meas.* vol. 32, no. 7, pp. 745–754, Jul. 2011.